Research Square

Preprints are preliminary reports that have not undergone peer review. They should not be considered conclusive, used to inform clinical practice, or referenced by the media as validated information.

Inhibition of papain-like protease PLpro blocks SARS-CoV-2 spread and promotes anti-viral immunity

Donghyuk Shin
Institute of Biochemistry II, Faculty of Medicine, Goethe University, Theodor-Stern-Kai 7, 60590 Frankfurt am Main, Germany.

Rukmini Mukherjee
Institute of Biochemistry II, Faculty of Medicine, Goethe University, Theodor-Stern-Kai 7, 60590 Frankfurt am Main, Germany.

Diana Grewe
Buchmann Institute for Molecular Life Sciences, Goethe University, Max-von-Laue-Str. 15, 60438 Frankfurt am Main, Germany

Denisa Bojkova
Institute of Medical Virology, University Hospital Frankfurt, Frankfurt am Main, Germany

Kheewoong Baek
Department of Molecular Machines and Signaling, Max Planck Institute of Biochemistry, Martinsried, Germany

Anshu Bhattacharya
Institute of Biochemistry II, Faculty of Medicine, Goethe University, Theodor-Stern-Kai 7, 60590 Frankfurt am Main, Germany.

Laura Schulz
Department of Theoretical Biophysics, Max Planck Institute of Biophysics, Max-von-Laue- Str. 3, 60438 Frankfurt am Main, Germany

Marek Widera
Institute of Medical Virology, University Hospital Frankfurt, Frankfurt am Main, Germany

Ahmad Reza Mehdipour
Department of Theoretical Biophysics, Max Planck Institute of Biophysics, Max-von-Laue- Str. 3, 60438 Frankfurt am Main, Germany

Georg Tascher
Institute of Biochemistry II, Faculty of Medicine, Goethe University, Theodor-Stern-Kai 7, 60590 Frankfurt am Main, Germany.

Paul P. Geurink
Oncode Institute and Department of Chemical Immunology, Leiden University Medical Centre, Einthovenweg 20, 2333 ZC, Leiden, The Netherlands

Gerbrand J. van der Heden van Noort
Oncode Institute and Department of Chemical Immunology, Leiden University Medical Centre, Einthovenweg 20, 2333 ZC, Leiden, The Netherlands
Huib Ovaa
Oncode Institute and Department of Chemical Immunology, Leiden University Medical Centre, Einthovenweg 20, 2333 ZC, Leiden, The Netherlands
Klaus- Peter Knobeloch
Institute of Neuropathology, Faculty of Medicine, University of Freiburg, Freiburg, Germany.
Krishnaraj Rajalingam
Cell Biology Unit, University Medical Center of the Johannes Gutenberg University Mainz, 55131 Mainz, Germany.
Brenda A. Schulman
Department of Molecular Machines and Signaling, Max Planck Institute of Biochemistry, Martinsried, Germany
Jindrich Cinatl
Institute of Medical Virology, University Hospital Frankfurt, Frankfurt am Main, Germany
Gerhard Hummer
Department of Theoretical Biophysics, Max Planck Institute of Biophysics, Max-von-Laue- Str. 3, 60438 Frankfurt am Main, Germany
Sandra Ciesek
Institute of Medical Virology, University Hospital Frankfurt, Frankfurt am Main, Germany
Ivan Dikic (dikic@biochem2.uni-frankfurt.de)
Institute of Biochemistry II, Faculty of Medicine, Goethe University, Theodor-Stern-Kai 7, 60590 Frankfurt am Main, Germany.

Research Article

Keywords: SARS-CoV-2, papain-like protease, biochemical structural and functional characterizations

Posted Date: May 5th, 2020

DOI: https://doi.org/10.21203/rs.3.rs-27134/v1

License: This work is licensed under a Creative Commons Attribution 4.0 International License.
Read Full License

Version of Record: A version of this preprint was published on July 29th, 2020. See the published version at https://doi.org/10.1038/s41586-020-2601-5.

Abstract

Main protease and papain-like protease (PLpro) are essential coronaviral enzymes required for polypeptide processing during viral maturation. PLpro additionally cleaves proteinous post-translational modifications from host proteins to evade anti-viral immune responses. Here, we provide biochemical, structural and functional characterizations of PLpro from SARS-CoV-2 (PLproCoV2) and reveal differences to that of SARS (PLproSARS) in controlling interferon (IFN) and NF-kB pathways. PLproCoV2 and PLproSARS share 83% sequence identity, yet they differ in their host substrate preferences: PLproCoV2 predominantly cleaves the ubiquitin-like protein ISG15 off from host proteins, while PLproSARS preferentially targets ubiquitin chains. The crystal structure of PLproCoV2 in complex with ISG15 explains the affinity and higher specificity through distinctive binding to ISG15's unique amino-terminal ubiquitin-like domain, and enabled the identification of GRL-0617 as a non-covalent candidate inhibitor for PLproCoV2. In human cells, PLproCoV2 cleaves ISG15 from interferon responsive factor 3 (IRF3), blocks its nuclear translocation, and reduces type I interferon responses, whereas PLproSARS preferentially mediates deubiquitination of critical components of the NF-kB pathway. Pharmacological inhibition of PLproCoV2 blocks the virus-induced cytopathogenic effect upon infection with SARS-CoV-2, fosters the anti- viral interferon pathway and reduces viral release from infected cells. We propose that therapeutic targeting of PLproCoV2 can suppress SARS-CoV-2 infection and promote anti-viral immunity.

Introduction

A novel coronavirus named Severe Acute Respiratory Syndrome CoronaVirus 2 (SARS–CoV-2) caused a worldwide outbreak of the respiratory disease COVID–19 by the beginning of 20201. COVID–19 generally has less severe symptoms and lower mortality rate, but is more infectious than the related Severe Acute Respiratory Syndrome (SARS) virus or Middle East Respiratory Syndrome (MERS), which caused global outbreaks in 2003 and 2012, respectively. The genome of SARS-CoV–2 shares about 80% sequence identity with SARS2,3. Both viruses critically rely on the activity of viral proteases: main protease (Mpro or 3CLpro) and papain- like protease (PLpro), which are essential for the processing of viral polypeptides, a critical for virus maturation, release and further spread 4,5. The main protease of SARS-CoV–2 has been studied and several small molecule inhibitors of its catalytic activity have been proposed as potential therapeutics 6–8. By contrast, the role of PLproCoV2 during infection and also in regulating host immune responses has not been studied in detail. This is particularly relevant as previous studies with PLproSARS indicate that it acts as a protease for ubiquitin and ubiquitin- related proteins, such as ISG15, which are known regulators of critical innate immune pathways 9–12.

Results And Discussion

The PLpro from SARS-CoV2 preferentially catalyses cleavage of ISGylated proteins

PLproSARS and PLproCoV2 are closely related, with 82.9% sequence identity, and relatively distant from PLproMERS (32.9% identity) (Extended data Fig. 1a). Nevertheless, PLproSARS and PLproCoV2 show clear differences in their substrate preferences, cleaving ubiquitinated and ISGylated substrates in HeLa cells treated with interferon (IFN)-β, respectively (Fig. 1a). PLproSARS strongly reduced the smears of ubiquitinated proteins and ISGylation of substrates, whereas PLproCoV2 preferentially reduced ISGylation of protein substrates (Fig. 1a).

We established purified systems and compared the reactions of both PLpros towards activity- based probes (ABPs) with propargyl (Prg) warheads at either the C-terminus of ubiquitin (Ub, K63- or K48-linked di-ubiquitin (K63 Ub_2, K48 Ub_2)), or several ubiquitin-like modifiers (ISG15, Nedd8 and SUMO1/2/3 13–17) (Fig. 1b, Extended data Fig. 1b). PLproCoV2 preferentially reacted with ISG15-based ABP, showed weak activity towards K48-linked di- ubiquitin and Nedd8, and no activity towards SUMO-based probes. In contrast, PLproSARS reacted most potently with Ub and K48-linked di-ubiquitin ABPs, but was less reactive toward the ISG15 probe (Fig. 1b, Extended data Fig. 1b). To confirm the differential preference of $PLpro^{CoV2}$ for ISG15, competition assays were performed with increasing doses of K48-Ub_2 (Fig. 1c). K48-Ub_2 effectively competed with ISG15-Prg reaction with $PLpro^{SARS}$ (left panel), but not with PLproCoV2 (right panel). Based on the ABP reactivities and sequence similarities between ubiquitin, ISG15, and NEDD8 (Extended data Fig. 1b, 1c), we also examined potential deneddylase activity of both PLproSARS and PLproCoV2 towards hyperneddylated CUL1. While neither removed the proximal NEDD8 linked to CUL1, both PLpro enzymes showed some activity towards hyperneddylation, a feature in common with the bonafide deneddylase DEN1 but not with the deubiquitylase USP2 (Fig. 1d). PLproSARS showed slightly greater deneddylating activity in this assay. Taken together, these results indicated that PLproCoV2 strongly prefers ISG15 as a cleavage substrate, whereas PLproSARS targets ubiquitin chains and to a lesser extent ISG15 and Nedd8.

Structural analysis of PLproCoV2 bound to ISG15

In order to understand the molecular basis for PLproCoV2 specificity towards ISG15, we determined the crystal structure of a PLproCoV2 (C111S)-ISG15 complex (murine ISG15, 63% sequence identity (73% similarity) to human ISG15) (Fig. 2a). Notably, ISG15 displays two tandem ubiquitin-like folds. The overall assembly of PLproCoV2 and both ISG15 domains was similar to the complex between PLproMERS with human ISG15 (Extended data Fig. 2a). The catalytic cysteine residue is also conserved with SARS (Extended data Fig. 2b). Compared to the crystal structure of ISG15 on its own, the N-terminal half of ISG15 is rotated by almost 90° and sits on the S2-helix of PLproCoV2 (Fig. 2b). A comparison with the structure of PLproSARS in complex with mISG15-C-term (PDB ID: 5TL7) showed that SARS and SARS-CoV–2 share the same binding mode to the C-lobe of mISG15 (Extended data Fig. 2c).

To gain insights into specificity, we compared the structure of the PLproCoV2-ISG15 complex to that of PLproSARS bound to K48-linked diubiquitin, where the distal ubiquitin is linked to the protease active site. The major difference between the two complexes is an interaction remote from the active site, with a protease S2 site binding the distal ubiquitin in the K48- linked chain, or the N-terminal ubiquitin-like fold in

ISG15. While PLproSARS Leu76 mediates a hydrophobic interaction with Ile44 on ubiquitin, the corresponding residue on PLproCoV2 is Thr75 (Fig. 2c-left). PLproCoV2 Val66 faces the hydrophobic patch (Ala2, Thr20, Met23) on ISG15's N-terminal ubiquitin fold domain (Fig. 2c-right). Intriguingly, both PLpro enzymes share Phe (PLproCoV2 Phe69 and PLproSARS Phe70) as the core residue to make hydrophobic interactions with either ubiquitin or ISG15. Introducing mutations on either Phe69 or Val66 on PLproCoV2 significantly decreased the enzymatic activity and showed less reactivity with ISG15-Prg compared to the wild-type (Fig. 2d), indicating that the S2 region determines the substrate specificity. We also found subtle differences between the C-lobe binding modes of ubiquitin and ISG15 to PLpro (Extended data Fig. 2d).

Next, we investigated the interaction between PLproCoV2 and its two substrates, K48-Ub2 and mISG15, using molecular dynamics (MD) simulations (Fig. 2e). The N-lobe of K48-Ub2 dissociated from PLproCoV2 at ~300 ns (Fig. 2e-left). By contrast, the N-terminal domain of mISG15 remained stably bound at the same site in a 1μs long simulation of the complex between PLproCoV2 and mISG15 (Fig. 2e-right, Fig. 2f). Together, these results suggest that substrate specificity of PLproCoV2 toward ISG15 is determined by binding to N-terminal and C-terminal domains of ISG15.

GRL−0617 is an effective inhibitor of PLproCoV2

With the pressing urgency to identify novel therapeutic strategies for COVID−19, we used the structural information to select GRL−0617, a previously identified non-covalent inhibitor of PLproSARS, for initial investigations on PLproCoV2 (Fig. 3a) 18. Based on the binding mode of GRL−0617 or other known naphthalene inhibitors to PLproSARS 18−21, we assumed that the conserved Tyr268 of PLproCoV2 could also bind GRL−0617 to block the entry of the ISG15 C- terminus towards the protease catalytic cleft (Fig. 3b). Indeed, IC_{50} of GRL−0617 to $PLpro^{CoV2}$ was similar to that of PLproSARS (0.74 ± 0.07 μM, 0.66 ± 0.08 μM, respectively, Fig. 3c). Interestingly, this inhibitor was not able to inhibit PLproMERS, where Thr replaces Tyr at this conserved position (Fig. 3c). In accordance, the mutation of Tyr268 to Gly in PLproCoV2 (Y268G) strongly inhibited the ability of GRL−0617 to block its catalytic activity (Fig. 3c), indicating the critical role of Tyr268 on PLproCoV2 in the inhibitory action of GRL−0617 to PLproCoV2. MD simulations of GRL−0617 with PLproSARS and PLproCoV2 further confirmed a common binding mode with strong interactions between GRL−0617 and Tyr268 (Tyr 269 for SARS) (Extended data Fig. 3b and c). Next, we tested whether GRL−0617 would be able to inhibit the delSGylase or deubiquitinase activities towards cellular substrates. GRL−0617 effectively blocked PLproCoV2 leading to increased levels of ISGylated proteins in IFN-αtreated cell lysates (Fig. 3d). GRL−0617 also blocked the deubiquitination activity of PLproSARS (Fig. 3d). Intriguingly, the effects of GRL−0617 on Prg-probes to PLproCoV2 were more prominent with $ISG15_{C\text{-}term}$-Prg than $ISG15_{FL}$-Prg or ubiquitin versus K48-Ub_2 to $PLpro^{SARS}$ (Fig. 3e and Extended data Fig. 3d), consistent with the structural data indicating that the interaction between ISG15's N-terminal ubiquitin fold domain potentiates the interaction with PLproCoV2. These results showed that GRL−0617 is an effective inhibitor of PLproCoV2 and suggest that the tyrosine-mediated naphthalene-derived inhibitors for PLproSARS can be readily used as potential inhibitors for PLproCoV2.

PLpro regulates immune responses via IFN and NF-kB pathways

To understand the differences in the physiological roles of the PLpros between SARS and SARS-CoV–2 viruses, we analysed the interactome of both PLpros. In accordance to our biochemical data, PLproCoV2 interacted strongly with ISG15, whereas PLproSARS showed more pronounced interaction with ubiquitin (Fig. 4a, Extended Fig. 4b). In addition, PLproCoV2 enriched proteins related to interferon induction including PRKDC, NONO and ILF2 (Fig. 4a). PRKDC is a viral DNA sensor which activates the IRF3-TBK1 pathway in virus-infected cells 22. NONO is necessary for cGAS-mediated immune response in response to HIV viral DNA 23.

The ILF2/ILF3 complex is a known interactor of DNA-PKs and activates the Type I interferon response 24. Significant interactors of PLproCoV2 also included several ribonucleoproteins (HNRNPM, HNRNPK) which are involved in splicing of the host RNA, which was recently shown to be essential for SARS-CoV–2 replication in cells12. These proteins are also involved in formation of extracellular vesicles which are often hijacked for viral release 25. Moreover, ISGylation has been shown to impair exosome release and viral budding 26,27. We also identified Galectin1 as a significant interactor of PLproCoV2. Gal–1 has been shown to induce viral fusion with target cells during HIV infection 28. On the other hand, PLproSARS strongly associates with several SERPINS including SERPINB3 which is known to inhibit papain proteases 29,30.

Consistent with the mass spectrometry (MS), biochemical and structural analysis, the expression of PLproCoV2 strongly decreased ISGylation of cellular proteins following interferon stimulation (Extended Fig. 4a), including that of interferon regulatory factor 3 (IRF3), a critical component in the type 1 interferon pathway (Fig. 4c). During viral infection, cytosolic viral DNA leads to the formation of a complex comprising the proteins STING, TBK1 and IRF3 which leads to phosphorylation and nuclear translocation of IRF3 inducing transcription of type I interferons 31. Previous studies showed that PLproSARS interacts with IRF3 and STING thereby preventing the formation of the active signalling complex needed for IRF3 activation 32,33. Our studies showed that expression of PLproCoV2 and PLproSARS both lead to loss of ISGylation of IRF3, though the effect is more pronounced for PLproCoV2 (Fig. 4c). A decrease in phosphorylation of TBK1, IRF3 and nuclear translocation of IRF3 was detected in PLproSARS and PLproCoV2 wild-type expressing cells. Interestingly, the PLproCoV2 catalytic mutant (C111S) showed dominant negative effects on phosphorylation of IRF3 suggesting a potential role of protease-mediated delSGylation upstream of TBK1 (Extended data Fig. 4c, d). Phosphorylation of TBK1 also activates the NFκB pathway causing an upregulation of inflammatory signalling [ref]. Though expression of PLproSARS had less impact on ISG15- modification of IRF3 (Fig. 4c), it strongly attenuated degradation of IkB-*α*Fig. 4d, Extended data Fig. 4f). Also, PLproSARS caused a severe reduction in nuclear translocation of p65 in TNF- α treated cells (Extended data fig. 4e).

Viral RNA entry can be mimicked by poly (I:C) treatment which induces IFN- β expression 34. Interestingly, expression of PLproCoV2 more effectively decreased the level of IFN-β promotor activation when compared to PLproSARS and this inhibitory effect of both PLpro enzymes was neutralized by the GRL–

0617 treatment (Fig. 4e, Extended data Fig. 4g). On the other side, expression of PLproSARS predominantly deubiquitinated IkB-*α*and thus blocked the TNF-*α*induced NF-kB-p65 expression, which was also sensitive to treatment of GRL–0617 (Fig. 4f, Extended data Fig. 4h). Together, our findings indicate how two closely related coronaviruses (SARS and SARS-CoV–2) could differentially counteract the host-immune system by their PLpro enzymes.

Inhibition of PLproCoV2 blocks viral spread and increases activation of the IFN pathway To determine whether inhibiting the catalytic activity of PLproCoV2 can effectively block viral replication, CaCo–2 cells were infected with SARS-CoV–2 with or without GRL–0617 treatment (Fig. 5a). The inhibitory effect of GRL–0617 was measured by cytopathogenic effect (CPE) inhibition. It was previously shown that GRL–0617 can inhibit viral replication of SARS in Vero E6 cells 18. We observed a gradual dose-dependent inhibition of SARS-CoV–2 -induced CPE in the presence of GRL–0617 with 100 μM of GRL–0617 showing a nearly 100% CPE inhibitory effects (Fig 5b). In addition, the intracellular production of viral RNA and the release of viral particles from infected cells to the supernatant, as measured by genetic monitoring of released viral RNA (Fig 5d), was decreased upon treatment by GRL–0617 (Fig. 5c, 5d, respectively). This indicates that viral maturation and release can be affected by blocking the activity of PLproCoV2 *in vivo* by GRL–0617. We next wanted to test if GRL–0617 treatment of virus-infected cells can also impact the components of IFN pathways, ISGylation of IRF3 and phosphorylation of TBK1 that were previously shown to be inhibited by transfected PLproCoV2 in cells (Fig. 4). Interestingly, GRL–0617 treatment of SARS-CoV–2-infected cells led to a significant increase of IRF3 ISGylation (Fig. 5e), which has been previously shown to affect anti-viral immune response 35,36. Similarly, activation and phosphorylation of TBK1, a known virus-induced kinase in the IFN pathway, was also increased upon treatment of GRL–0617 during SARS-CoV–2 infection (Fig. 5f). These findings provide evidence that inhibition of PLproCoV2 *in vivo* can re-establish proper signalling via TBK1 and IRF3 and thus circumvent the immune evasion mechanism exerted via PLproCoV2 signalling. Indeed, GRL–0617 treatment significantly increased the ISG15 expression level from SARS-CoV–2 infected cells (Fig. 5g). Targeting of PLproCoV2 may thus have a dual effect in host cells—blocking the virus release and promoting antiviral IFN signalling (Fig. 5h).

Taken together, our data revealed structural and mechanistic understanding of PLproCoV2 actions during SARS-CoV–2 infection. PLproCoV2 and PLproSARS differ in their specificity toward cleaving ISG15 and ubiquitin chains, respectively. More importantly, such specificities correlated well with the ability of PLproCoV2 to block type I IFN, whereas PLproSARS reduced more preferentially the NF-*κ*B pathway. It is well established that inhibition of type 1 IFN pathway will impact on the initiation of anti-viral innate immunity, whereas inhibition of the NF-*κ*B pathway may lead to increased cell death and strong pro-inflammatory cytokine response involving TNF-*α*and IL–6 37–41. Such activities of PLpro enzymes in the epithelium, the prime site of infection entry, may in part contribute to release of cytokine flux and more aggressive and severe symptoms observed in SARS as compared to COVID–19 infections.

So far, the main protease of SARS-CoV–2 has been in the focus as the potential drug target against COVID–19 and several novel inhibitors have already been described 6–8. This is based on the rationale

that the main proteases of coronaviruses are essential for viral polypeptide processing and virus release. Yet, our results establish PLproCoV2 as an equally promising target for therapeutic intervention, being essential both for viral polypeptide processing and replication and dampening the innate immune responses by inhibiting the IFN pathway. Thus, therapeutic targeting of PLproCoV2 in the clinic may block SARS-CoV–2 maturation and promote anti-viral IFN signalling. Inhibitors of PLproCoV2, in particular naphthalene-based compounds such as GRL–0617, might be promising starting points for development of novel anti-COVID–19 therapeutics.

Methods

Plasmids construction

The papain-like protease domain sequence is obtained from SARS-CoV-2 complete genome (NCBI genome databank, Severe acute respiratory syndrome coronavirus 2 isolate Wuhan-Hu- 1, complete genome; NC_045512). Protein sequence for PLproCoV2 domain (amino acids, 746- 1060) of Nsp3 protein from SARS-CoV-2 (Nsp3; YP_009725299.1) was codon optimized, synthesized and cloned into pET28b with NcoI and XhoI to have C-terminal His-tag (Genescript). Protein sequences of PLpro domain of SARS and MERS from (PDB ID: 3MJ5, 5W8U, respectively) were also codon optimized, synthesized and cloned into pET28b with NcoI and XhoI to have C-terminal His-tag (Genescript). Mutants were generated by PCR and verified with sequencing. For mammalian expression, PLpros are cloned into pEGFP-C1 (clontech).

Protein purification

BL21(DE3) *E. coli* competent cells (NEB) were transformed with plasmids and grown in LB medium to an OD_{600} of 0.6-0.8 at 37°C. Recombinant murine ISG15 were kindly gifted from Dr. K.P. Knobeloch (University Freiburg). Protein expression was induced by addition of 0.5 mM IPTG (isopropyl $_D$-thiogalactopyranoside) and 1 mM Zinc Chloride ($ZnCl_2$) the cells were further grown overnight at 18°C and harvested. The cell pellet was resuspended in lysis buffer 50 mM Tris-HCl, 150 mM NaCl, 10 mM Imidazole, 2 mM DTT, pH 8.5) and lysed by sonication and centrifuged at 13,000 rpm to clarify the supernatant. The supernatant was incubated 2 hours with TALON beads (Takara) pre-equilibrated with lysis buffer and non- specific proteins were cleared with washing. Proteins were eluted with elution buffer (50 mM Tris-HCl, 150 mM NaCl, 250 mM Imidazole, 2 mM DTT, pH 8.5). Eluted proteins were buffer exchanged to storage buffer (20 mM Tris-HCl, 100 mM NaCl, 2 mM DTT, pH 8.5) and stored for biochemical analysis. For crystallization of PLproCoV2-C111S, the cell pellet was resuspended in lysis buffer (50 mM Tris-HCl, 150 mM NaCl, 10 mM Imidazole, 1 mM TCEP, pH 7.4) and lysed by sonication and centrifuged at 13,000 rpm to clarify the supernatant. The supernatant was incubated 2 hours with TALON beads (Takara) pre-equilibrated with lysis buffer and non-specific proteins were cleared with washing. Proteins were eluted with elution buffer (50 mM Tris-HCl, 150 mM NaCl, 250 mM Imidazole, 1 mM TCEP, pH 7.4) and further purified on size-exclusion column (Superdex 75 16/60, GE Healthcare) pre-

equilibrated with 20 mM Tris-HCl, 100 mM NaCl, 1 mM TCEP, pH7.4. Proteins were concentrated to 20 mg/ml and stored for crystallization.

Ubiquitin/NEDD8/SUMO-/ISG15 activity-based probes assay

PLPros were diluted (2 μM, final concentration) with activation buffer and incubated 10 minutes at 25°C and the activity-based probes were diluted (0.2 mg/ml, final concentration) in dilution buffer (50 mM Tris-HCl 7.5, 150 mM NaCl). The reaction mixture was prepared by mixing equal volume of activated PLpros (2 μM) and activity-based probes (0.2 mg/ml). Reactions were conducted at indicated temperature (on ice or 37°C) and samples were taken at the indicated time points and the reactions were quenched by the addition of SDS-sample buffer. Samples were further analyzed by SDS-PAGE and stained with silver staining kit (Thermo Fisher).

Crystallization

The equal amount of PLproCoV2-C111S were mixed with full-length murine ISG15. Final concentration of mixture was 250 μM. Protein mixture were screened with sitting drop matrix screens in 96-well plate with 100 nl of protein and 100 nl of precipitant solution at 293K. Initial crystals appeared from solution containing 20 % PEG 3350, 200 mM Potassium thiocyanate with 250 μM protein concentration. Diffraction-quality crystals were grown in optimized solution containing 18 % PEG 3350, 100 mM bis-tris propane pH 6.5, 200 mM Potassium thiocyanate with 200 μM protein concentration.

Data collection, processing and structure determination

Crystals were cryo-protected using mother liquor solution supplemented with 25 % (v/v) ethylene glycerol. Diffraction data were collected on single frozen crystal in a nitrogen stream at 100 K at beamline PXI as Swiss Light Source, Villigen. Initial data sets were processed using XDS 42, and phases were determined by Phaser molecular replacement in ccp4 module with PLproCoV2, mISG15 as template model 43, PDB IDs: 6W9C and 5TLA, respectively). Structure refinement and manual model building were performed with Coot and Phenix.Refine 44,45.

Cell lysates deubiquitination and deISGylation assay

HeLa or A549 cells were treated with IFN-β (200 U/ml) for 48 hrs to induce ISGylation. Cells were lysed with lysis buffer (50 mM Tris-HCl (pH 8.0), 150 mM NaCl, 1% (v/v) NP-40) and concentration was measured with BCA assay (Thermo Fischer). 10 μg of lysates were incubated with 100 nM of PLpro for

indicated timepoints at 37°C and analyzed by immunoblotting with indicated antibodies. To test inhibitory effect of GRL-0617, 40 μM of GRL-0617 was included during reaction.

Deneddylation and I*k*B*a* deubiquitination assay

All proteins described are of human origin. CUL1-RBX1, SKP1-*b*-TRCP2, UBE2M, UBE2D3, NEDD8, UB, APPBP1-UBA3, UBA1 were purified as previous described 46. Neddylated CUL1-RBX1 was generated as previous described 46. Reaction for generating hyperneddylated CUL1-RBX1 was driven at pH 8.8 at 37°C for 30 min, and purified size exclusion chromatography. USP2 catalytic core was purified with nickel affinity chromatography, liberated of the His-tag by overnight thrombin cleavage, following IEX and size exclusion chromatography. CSN was purified as previous described 47. Deneddylation assays were performed with 1 μM hyperneddylated CUL1-RBX1, and 5μM protease (PLproSARS, PLproCoV2, DEN1, USP2) or 20 nM CSN. Reaction was performed at 37°C in 2 5mM Tris 100 mM NaCl, 5 mM DTT pH 8.5, and in the case of CSN with additional 10mM $MgCl_2$. Samples were taken each indicated time points and quenched with 2X SDS-PAGE sample buffer. Gels were stained by coomassie-blue and scanned on an Amersham imager 600. I*k*B*a* Deubiquitylation assays were performed by first generating a ubiquitylated I*k*B*a*, with 200 nM UBA1, 1 μM UBE2D3, 20 μM UB, 500 nM neddylated CRL1β-TRCP, and 5μM fluorescently labelled I*k*B*a* at 37°C in 50 mM Tris 50mM NaCl 10mM $MgCl_2$ 5mM DTT pH 7.5 for 30 minutes. Reaction was quenched by adding 80mM EDTA for 5 minutes. Deubiquitylation reaction was started by mixing 3 μM of protease (PLproSARS, PLproCoV2, USP2) with the ubiquitylation reaction, and samples were taken each time points and quenched with 2X SDS- PAGE sample buffer. Gels were scanned on an Amersham Typhoon (GE) detecting the fluorescently labelled I*k*B*a*.

Molecular Dynamics Simulations

PLproCoV2 with K48-Ub2:

For the model of PLproCoV2 with bound K48-Ub2, we combined the X-ray crystal structure of the apo form (PDB ID: 6W9C, re-refined by Tristan Croll (https://drive.google.com/drive/folders/1JBo50CdkBU7K1pFThuqrzhQ-NcsIAWyG) with the substrate coordinates taken from PDB ID: 5E6J48 after PLpro alignment using PyMol 49. The triazole linker was replaced with Lys using MODELLER 50. To mimic the linker, a harmonic distance restraint potential was applied between the backbone carbonyl carbon atoms of Lys48 and Gly75 with a target distance of 9.5 Å and a force constant of 502080 kJ mol−1 nm−2. The covalent propargylamide linker was removed.

PLproSARS and PLproCoV2 in complex with inhibitor GRL-0617:

The coordinates of the PLproSARS complex were taken from PDB ID: 3E9S 18. The oxidized Cys112 was changed to the reduced form (SH) using MODELLER. The simulation model of the PLproCoV2 complex was built according to the X-ray structure of the apo form (PDB ID: 6W9C, re-refined by Tristan Croll). The

coordinates of the compound GRL-0617 were modeled according to PDB ID: 3E9S after PLpro alignment using PyMol. The loop (GNYQCGH) capping the GRL-0617 binding site was remodeled according to the PLproSARS X-ray crystal structure of the complex (PDB ID: 3E9S) using MODELLER. The GRL-0617 ligand was parameterized with the General Amber Force Field (GAFF) 51.

PLproCoV2 with mISG15:

The X-ray crystal structure PLproCoV2:mISG15 served as starting point. Missing residues of PLproCoV2 and one Zn ion were modeled according to the apo X-ray crystal structure (PDB ID: 6W9C, re-refined by Tristan Croll). Missing side chains in all setups were modeled using MODELLER. All crystallographic water molecules and ions were retained, except a nickel ion in PDB ID: 5E6J. According to pKa calculations using PropKa and additional visual inspections, in all setups His17CoV2 (His18SARS) and His272 CoV2 (His273SARS) were charged. All other residues were simulated in their physiological protonation state. The proteins were solvated in TIP4P-D water 52 with 150 mM NaCl. MD simulations were carried out using Gromacs 2018 53 and the AMBER99SB*-ILDN-q force field 54–57. Each system was energy minimized, followed by five equilibration steps, in which we gradually weakened the position restraints on heavy atoms, first in an NVT ensemble (0.25 ns) and then in an NPT ensemble (4 x 0.5 ns) using a Berendsen thermostat and barostat 58. Production simulations of 1 µs each were run at a temperature of 310 K and a pressure of 1 bar in an NPT ensemble using a Nosé- Hoover thermostat 59,60 and a Parrinello-Rahman barostat 61. For simulations with bound substrates and with bound inhibitor, we monitored the root-mean-square deviation (RMSD) of each backbone substrate (distal ubiquitin in K48-Ub2 and N-terminal domain of mISG15) and of GRL-0617 (heavy atoms) to the respective equilibrated structure after alignment on the helix backbone of PLpro (without the flexible UBL domain).

Inhibitor IC_{50} determination

For IC_{50} value for inhibitors, ubiquitin-AMC was used as substrate of PLpro and the release of AMC was measured by increase of fluorescence (Ex./Em. 360/487 nm) on 384-well microplate reader (PHERAstar FSX, BMG Labtech). 5ul of solution containing different concentration of GRL-0617 (200 – 0 µM) and 10 µM of ubiquitin-AMC were aliquoted into 384 well plate and reaction was initiated by addition of 5 µl of PLpro (30 nM) to the well. Initial velocities of AMC-release were normalized against to DMSO control. IC_{50} value is calculated by Dose- response – Inhibition function in Graphpad Prism with [inhibitor] vs normalized response equation. The experiment was repeated three times.

Mass-spectrometry

For interactome analysis, A549 cells were transfected with CoV2 mut PLpro/wt and for comparison between SARS and SARS-CoV-2, mutant PLpro versions for both proteins were transfected. Cells were stimulated with Interferon-β (200 units/ml) for 36 hours to mimic infection scenario. Cells were lysed in ice cold lysis buffer (50 mM Tris-Cl, pH 7.5; 150 mM NaCl; 1% Triton x-100) and equal amounts of lysates

were incubated with GFP nanotrap beads in IP buffer (Lysis buffer without detergent). After incubation, IPs were washed three times with wash buffer (50 mM Tris-Cl, pH7.5; 400 mM NaCl; 0.5 mM EDTA) and two times with IP buffer. Then beads were incubated with 25 ul of 50 mM tris-HCl (pH 8.5) containing 4 M urea, 1 mM Tcep, 4 mM Chloroacetamide for 1 hour in dark at 37°C. Afterwards, samples were then diluted with 50 mM Tris-cl pH 8.5 to final urea conc. < 2M and digested with 0.5 µg Trypsin (Promega) at 37°C overnight. Digests were acidified using trifluoroaceticacid (TFA) to a pH of 2-3 and peptides were enriched using stage tips 62. For getting quantitative information, peptides were labelled with TMT reagents (Thermo fisher) as described previously63. Briefly, peptides were resuspended in TMT labelling buffer (0.2 M EPPS pH 8.2, 20% Acetonitrile) and were mixed with TMT reagents in a 2:1 TMT : peptide ratio. Reaction was performed for one hour at RT and subsequently quenched by addition of hydroxylamine to a final concentration of 0.5% at RT for 15min. Samples were pooled in equimolar ratio, acidified, and cleaned up using Empore C18 (Octadecyl) resin material. After drying, peptides were resuspended in 0.1% FA for LC-MS. All mass spectrometry data was acquired in centroid mode on an Orbitrap Fusion Lumos mass spectrometer hyphenated to an easy-nLC 1200 nano HPLC system with a nanoFlex ion source (ThermoFisher Scientific). A spray voltage of 2.6 kV was applied with the transfer tube heated to 300°C and funnel RF set to 30%. Internal mass calibration was enabled (lock mass 445.12003 m/z). Peptides were separated on a self-made 32 cm long, 75 µm ID fused-silica column, packed in house with 1.9 µm C18 particles (ReproSil-Pur, Dr. Maisch) and heated to 50°C using an integrated column oven (Sonation). HPLC solvents consisted of 0.1% Formic acid in water (Buffer A) and 0.1% Formic acid, 80% acetonitrile in water (Buffer B). Peptides were eluted by a non-linear gradient from 7 to 40% B over 90 minutes followed by a step-wise increase to 95% B in 6 minutes which was held for another 9 minutes. Full scan MS spectra (350-1400 m/z) were acquired with a resolution of 120,000 at m/z 200, maximum injection time of 100 ms and AGC target value of 4 x 105. The 20 most intense precursors per full scan with a charge state between 2 and 5 were selected for fragmentation (“Top 20”), isolated with a quadrupole isolation window of 0.7 Th and fragmented via HCD applying an NCE of 38%. MS2 scans were performed in the Orbitrap using a resolution of 50,000 at m/z 200, maximum injection time of 86ms and AGC target value of 1 x 105. Repeated sequencing of already acquired precursors was limited by setting a dynamic exclusion of 60 seconds and 7 ppm and advanced peak determination was deactivated. MS raw data was analysed with Proteome Discoverer (PD, version 2.4, ThermoFisher Scientific) using Sequest HT as a search engine and performing re-calibration of precursor masses by the Spectrum RC-node. Fragment spectra were searched against the human reference proteome (“one sequence per Gene”, 20531 sequences, version March 2020) and protein sequences for SARS (15 sequences, version March 2020), CoV2 (14 sequences, version February 2020) and MERS (10 sequences, version April 2020) downloaded from Uniprot in March 2020 as well as common contaminants as included in “contaminants.fasta” provided with the MaxQuant software. Static modifications were TMT at the peptide N-terminus and lysines as well as carbamidomethyl at cysteine residues, dynamic modifications were set as Oxidation of Methionine and Acetylation at the protein-N-term. Matched spectra were filtered with Percolator applying a false discovery rate of 1% on PSM and protein level. Reporter intensities were normalised to the total protein intensities in PD assuming equal sample loading and additionally by median-normalisation using the NormalyzerDE package 64. Statistically significant

changes between samples were determined in Perseus (version 1.6.6.0) using a Two-sample T-test with a Benjamini-Hochberg FDR of 5% on log2 transformed values 65.

Cell culture

Human CaCo–2 cells were obtained from the Deutsche Sammlung vonMikroorganismen und Zellkulturen (DSMZ; Braunschweig, Germany). Cells were grown at 37°C in Minimal Essential Medium (MEM) supplemented with 10% fetal bovine serum (FBS) and containing 100 IU/ml penicillin and 100 µg/ml streptomycin.

Virus preparation

SARS-CoV–2/FFM1 was isolated from asymptomatic travellers returning from Wuhan (China) to Frankfurt (Germany) using CaCo–2 cells. SARS-CoV–2/FFM1 stocks used in the experiments had undergone one passage on CaCo–2 cells. Virus titers were determined as TCID50/ml in confluent cells in 96-well microtiter plates.

Antiviral and cytotoxicity assays

Confluent layers of CaCo–2 cells in 96-well plates were infected with SARS-CoV–2/FFM1 at MOI 0.01. Virus was added simultaneously with GRL-0617 and incubated in MEM supplemented with 1% FBS with different drug dilutions. Cytopathogenic effect (CPE) was assessed visually 48 h after infection. To assess effects of GRL-0617 on CaCo–2 cell viability, confluent cell layers were treated with different drug concentration. Cell viability was determined by 3-(4,5-dimethylthiazol-2-yl)-2,5-549 diphenyltetrazolium bromide (MTT) assay modified after Mosman 66, as previously described 67. Data for each condition was collected for at least three biological replicates.

Luciferase activity assay

To analyze the induction of IFNβ induced genes, a luciferase reporter assay was used in A549 cells. Briefly, an expression construct containing the luciferase ORF and the IFNβ promoter (IFNβ/luciferase) was co-transfected with either a GFP control plasmid or the designated PLpro plasmid. For all transfections, 100 ng of luciferase plasmid, 400ng of Plpro or GFP vector was used in each well of a 12 well plate All transfections were performed in triplicate and the average of 3 experiments is shown in figures. 24h post transfection cells were treated with 500ng poly I:C for 18h or 50ng/ml of TNFα for 30min. Luciferase expression was measured Luciferase Reporter assay system (Promega Inc). Fold change is calculated by taking vector treated with poly I:C or TNF-α as 1.

Immunofluorescence and confocal imaging

HeLa cells expressing GFP tagged PLPro was treated with TNFα (50ng/ml) for 45min. Cells were fixed with paraformaldehyde, blocked in 5% serum and immunostained overnight at 4°C with antibody against p65. Confocal imaging was performed using the Zeiss LSM780 microscope system. An Ar-ion laser (for excitation of GFP at 488 nm), a He-Ne laser (for excitation Alexa Fluor 546nm) were used with a 63×1.4 NA oil immersion objective. Images were analysed in FIJI to check for colocalisation between DAPI and immunostained p65. Results are indicative of 50 cells taken from 3 independent experiments; error bars indicate standard deviation.

Nuclear Fractionation

A549 cells from a confluent 60 mm dish were transiently transfected with GFP tagged PLPro followed by treatment with interferonα (200u/ml, 36h). Cells were lysed in hypotonic buffer [10 mmol/L HEPES (pH = 7.4), 2 mmol/L MgCl2, 25 mmol/L KCl, 1 mmol/L DTT, 1 mM PMSF, and protease inhibitor cocktail], kept on ice for 30 min followed by syringe lysis, 2 mol/L sucrose solution was added dropwise, followed by centrifugation at 1000g for 15 min. The supernatant was saved as the cytosolic fraction. The pellet was washed twice in wash buffer [10 mmol/L HEPES (pH = 7.4), 2 mmol/L $MgCl_2$, 25 mmol/L KCl, 250 mmol/L sucrose, 1 mmol/L DTT, 1 mmol/L PMSF, and protease inhibitor cocktail] and saved as the nuclear fraction.

Quantification of viral and cellular RNA

SARS-CoV-2 RNA from cell culture supernatant samples was isolated using ACL buffer and the QIAamp 96 Virus kit (Qiagen) according to the manufacturer's instructions. RNA was subjected to OneStep qRT-PCR analysis using the LightCycler Multiplex RNA Virus Master kit (Roche). Intracellular RNA was isolated using RLT buffer and the RNeasy 96 HT Kit according to the manufacturer's instructions. PCR was performed on a CFX96 Real-Time System, C1000 Touch Thermal Cycler. Primers and probe were adapted from the WHO protocol 68 targeting the open reading frame for RNA-dependent RNA polymerase (RdRP) of both SARS-CoV-2: RdRP_SARSr-F2 (GTGARATGGTCATGTGTGGCGG) andRdRP_SARSr-R1 (CARATGTTAAASACACTATTAGCATA) primers were used in a final concentration of 0.4 μM and RdRP_SARSr_P2 probe (6-Fam CAGGTGGAACCTCATCAGGAGATGC BBQ1) was used with 0.2 μM, respectively. Primers for ACTB (fwd:CATCGAGCACGGCATCGTCA; rev:TAGCACAGCCTGGATAGCAAC) 69 and ISG15 (fwd: GAGAGGCAGCGAACTCATCT; rev: AGGGACACCTGGAATTCGTT) 70 were used for SYBR green based detection of cellular genes in a final concentration of 0.4 μM per reaction. For each condition, three biological replicates were used. Mean and standard deviation were calculated for each group.

Declarations

Acknowledgements

We thank Daniela Hoeller and Kerstin Koch for critical comments on the manuscript. We also thank Swiss Light Source (SLS) for providing special beamtime for this project during the peak of the Covid-19 pandemic in Switzerland and Wang Meitian and Olieric Vincnet for providing on-site support during the data collection. This work was supported by the DFG-funded Collaborative Research Centre on Selective Autophagy (SFB 1177), by the Max Planck Society, by NWO (H.O. and G.J.v.d.H.v.N.) by the European Research Council (ERC) under the European Union's Horizon 2020 research and innovation programme (grant agreement No 789016) to BAS and (grant agreement No 742720) to I.D., by the grants from Else Kroener Fresenius Stiftung, Dr. Rolf M. Schwiete Stiftung, and by internal IBC2 funds to (I.D.).

Author contributions

DS and ID conceived the project. DS contributed protein purification, biochemical and biophysical activity assay and structure determination. RM performed cell biology experiments. DG contributed protein purification. DB contributed virus infection experiments, MW was doing RT-PCR measurements, KB performed deneddylation assay. AB and GT designed, performed mass spectrometry experiments and analyzed data. LS and ARM performed MD simulations. PPG and GJvdHvN synthesized -probes in the lab of HO. BS, GH, JC, SC and ID supervised the project. DS and ID analyzed the data and wrote the manuscript with input from all the co-authors.

Author information

Mass spectrometry data will be deposited in the Proteomics Identification (PRIDE) database. Reprints and permissions information is available at www.nature.com/reprints. The authors declare no competing financial interests. Correspondence to I. D. (Ivan.Dikic@biochem2.de)

Data availability

The atomic coordinate of PLpro-ISG15 (murine) has been deposited in the PDB with accession code 6YVA in the Protein Data Bank.

References

1. Huang, C. *et al.* Clinical features of patients infected with 2019 novel coronavirus in Wuhan, China. *Lancet* **395**, 497–506 (2020).
2. Lu, R. *et al.* Genomic characterisation and epidemiology of 2019 novel coronavirus: implications for virus origins and receptor binding. *Lancet* **395**, 565–574 (2020).

3. Zhou, P. *et al.* A pneumonia outbreak associated with a new coronavirus of probable bat origin. *Nature* **579**, 270–273 (2020).
4. Lim, K. P., Ng, L. F. P. & Liu, X. Identification of a Novel Cleavage Activity of the First Papain-Like Proteinase Domain Encoded by Open Reading Frame 1a of the Coronavirus Avian Infectious Bronchitis Virus and Characterization of the Cleavage Products. *J. Virol.* **74**, 1674–1685 (2000).
5. Harcourt, H. *et al.* Identification of Severe Acute Respiratory Syndrome Coronavirus Replicase Products and Characterization of Papain-Like Protease Activity. *J. Virol.* **78**, 13600–13612 (2004).
6. Zhang, L. *et al.* Crystal structure of SARS-CoV-2 main protease provides a basis for design of improved α-ketoamide inhibitors. *Science (80-.).* **368**, 409–412 (2020).
7. Jin, Z. *et al.* Structure of Mpro from COVID-19 virus and discovery of its *Nature* (2020) doi:10.1038/s41586-020-2223-y.
8. Dai, W. *et al.* Structure-based design of antiviral drug candidates targeting the SARS- CoV-2 main protease. *Science (80-.).* **eabb4489**, (2020).
9. Hermanns, T. & Hofmann, K. Bacterial dubs: Deubiquitination beyond the seven classes. *Biochemical Society Transactions* (2019) doi:10.1042/BST20190526.
10. Shin, *et al.* Regulation of Phosphoribosyl-Linked Serine Ubiquitination by Deubiquitinases DupA and DupB. *Mol. Cell* (2019) doi:10.1016/j.molcel.2019.10.019.
11. Sánchez-Martín, P., Saito, T. & Komatsu, M. p62/ <scp>SQSTM</scp> 1: ‘Jack of all trades’ in health and cancer. *FEBS* **286**, 8–23 (2019).
12. Bojkova, D. *et al. SARS-CoV-2 infected host cell proteomics reveal potential therapy targets*. *Research Square* (2020) doi:10.21203/rs.3.rs-17218/v1.
13. Sommer, S., Weikart, D., Linne, U. & Mootz, H. D. Covalent inhibition of SUMO and ubiquitin-specific cysteine proteases by an in situ thiol–alkyne addition. *Bioorg. Med. Chem.* **21**, 2511–2517 (2013).
14. Ekkebus, R. *et al.* On Terminal Alkynes That Can React with Active-Site Cysteine Nucleophiles in Proteases. *Am. Chem. Soc.* **135**, 2867–2870 (2013).
15. Flierman, D. *et al.* Non-hydrolyzable Diubiquitin Probes Reveal Linkage-Specific Reactivity of Deubiquitylating Enzymes Mediated by S2 Pockets. *Cell Chem. Biol.* **23**, 472–482 (2016).
16. Basters, A. *et al.* Structural basis of the specificity of USP18 toward ISG15. *Struct. Mol. Biol.* **24**, 270–278 (2017).
17. Geurink, P. P. *et al.* Profiling DUBs and Ubl-specific proteases with activity-based probes. in *Methods in Enzymology* 357–387 (2019). doi:10.1016/bs.mie.2018.12.037.
18. Ratia, K. *et al.* A noncovalent class of papain-like protease/deubiquitinase inhibitors blocks SARS virus replication. *Natl. Acad. Sci.* **105**, 16119–16124 (2008).
19. Báez-Santos, Y. M. *et al.* X-ray Structural and Biological Evaluation of a Series of Potent and Highly Selective Inhibitors of Human Coronavirus Papain-like Proteases. *Med. Chem.* **57**, 2393–2412 (2014).

20. Ghosh, A. *et al.* Severe Acute Respiratory Syndrome Coronavirus Papain-like Novel Protease Inhibitors: Design, Synthesis, Protein−Ligand X-ray Structure and Biological Evaluation. *J. Med. Chem.* **53**, 4968–4979 (2010).
21. Ghosh, A. *et al.* Structure-Based Design, Synthesis, and Biological Evaluation of a Series of Novel and Reversible Inhibitors for the Severe Acute Respiratory Syndrome−Coronavirus Papain-Like Protease. *J. Med. Chem.* **52**, 5228–5240 (2009).
22. Ferguson, B. J., Mansur, D. S., Peters, E., Ren, H. & Smith, G. L. DNA-PK is a DNA sensor for IRF-3-dependent innate immunity. *Elife* **1**, e00047 (2012).
23. Lahaye, X. *et al.* NONO Detects the Nuclear HIV Capsid to Promote cGAS-Mediated Innate Immune Activation. *Cell* **175**, 488-501.e22 (2018).
24. Watson, S. F., Bellora, N. & Macias, S. ILF3 contributes to the establishment of the antiviral type I interferon program. *Nucleic Acids Res.* **48**, 116–129 (2020).
25. Leidal, A. M. *et al.* The LC3-conjugation machinery specifies the loading of RNA- binding proteins into extracellular vesicles. *Cell Biol.* **22**, 187–199 (2020).
26. Okumura, A., Pitha, P. M. & Harty, N. ISG15 inhibits Ebola VP40 VLP budding in an L-domain-dependent manner by blocking Nedd4 ligase activity. *Proc. Natl. Acad. Sci.* **105**, 3974–3979 (2008).
27. Villarroya-Beltri, C. *et al.* ISGylation controls exosome secretion by promoting lysosomal degradation of MVB proteins. *Commun.* **7**, 13588 (2016).
28. Ouellet, M. *et al.* Galectin-1 Acts as a Soluble Host Factor That Promotes HIV-1 Infectivity through Stabilization of Virus Attachment to Host Cells. *Immunol.* **174**, 4120–4126 (2005).
29. Schick, C. *et al.* Cross-Class Inhibition of the Cysteine Proteinases Cathepsins K, L, and S by the Serpin Squamous Cell Carcinoma Antigen 1: A Kinetic Analysis †. *Biochemistry* **37**, 5258–5266 (1998).
30. Takeda, A., Yamamoto, T., Nakamura, Y., Takahashi, T. & Hibino, T. Squamous cell carcinoma antigen is a potent inhibitor of cysteine proteinase cathepsin L. *FEBS Lett.* **359**, 78–80 (1995).
31. Tanaka, Y. & Chen, Z. J. STING Specifies IRF3 Phosphorylation by TBK1 in the Cytosolic DNA Signaling Pathway. *Signal.* **5**, ra20–ra20 (2012).
32. Devaraj, S. G. *et al.* Regulation of IRF-3-dependent Innate Immunity by the Papain- like Protease Domain of the Severe Acute Respiratory Syndrome Coronavirus. *Biol. Chem.* **282**, 32208–32221 (2007).
33. Sun, L. *et al.* Coronavirus Papain-like Proteases Negatively Regulate Antiviral Innate Immune Response through Disruption of STING-Mediated Signaling. *PLoS One* **7**, e30802 (2012).
34. Sheikh, F., Dickensheets, H., Gamero, A. M., Vogel, S. & Donnelly, R. P. An essential role for IFN-β in the induction of IFN-stimulated gene expression by LPS in macrophages. *J. Leukoc. Biol.* **96**, 591–600 (2014).
35. Shi, H.-X. *et al.* Positive Regulation of Interferon Regulatory Factor 3 Activation by Herc5 via ISG15 Modification. *Cell. Biol.* **30**, 2424–2436 (2010).

36. Lu, G. *et al.* ISG15 enhances the innate antiviral response by inhibition of IRF-3 degradation. *Mol. Biol.* **52**, 29–41 (2006).
37. Baker, R. G., Hayden, M. S. & Ghosh, S. NF-κB, Inflammation, and Metabolic Disease. *Cell Metab.* **13**, 11–22 (2011).
38. Lawrence, T. The Nuclear Factor NF- B Pathway in *Cold Spring Harb. Perspect. Biol.* **1**, a001651–a001651 (2009).
39. Stetson, D. B. & Medzhitov, Type I Interferons in Host Defense. *Immunity* **25**, 373– 381 (2006).
40. Teijaro, J. R. Type I interferons in viral control and immune regulation. *Opin. Virol.* **16**, 31–40 (2016).
41. Lee, A. J. & Ashkar, A. A. The Dual Nature of Type I and Type II Interferons. *Immunol.* **9**, (2018).
42. Kabsch, W. XDS. *Acta Crystallogr. Sect. D Biol. Crystallogr.* **66**, 125–132 (2010).
43. McCoy, A. J. *et al.* Phaser crystallographic software. *Appl. Crystallogr.* **40**, 658–674 (2007).
44. Afonine, P. *et al.* Towards automated crystallographic structure refinement with phenix.refine. *Acta Crystallogr. Sect. D Biol. Crystallogr.* **68**, 352–367 (2012).
45. Emsley, P., Lohkamp, B., Scott, W. & Cowtan, K. Features and development of Coot. *Acta Crystallogr. Sect. D Biol. Crystallogr.* **66**, 486–501 (2010).
46. Baek, K. *et al.* NEDD8 nucleates a multivalent cullin–RING–UBE2D ubiquitin ligation assembly. *Nature* **578**, 461–466 (2020).
47. Enchev, R. I. *et al.* Structural Basis for a Reciprocal Regulation between SCF and CSN. *Cell Rep.* **2**, 616–627 (2012).
48. Békés, M. *et al.* Recognition of Lys48-Linked Di-ubiquitin and Deubiquitinating Activities of the SARS Coronavirus Papain-like Protease. *Cell* **62**, 572–585 (2016).
49. Schrödinger, L. The PyMol Molecular Graphics System, Versión 1.8. *Thomas Holder* (2015) doi:10.1007/s13398-014-0173-7.2.
50. Šali, & Blundell, T. L. Comparative Protein Modelling by Satisfaction of Spatial Restraints. *J. Mol. Biol.* **234**, 779–815 (1993).
51. Wang, J., Wolf, R. M., Caldwell, J. W., Kollman, P. & Case, D. A. Development and testing of a general amber force field. *J. Comput. Chem.* **25**, 1157–1174 (2004).
52. Piana, S., Donchev, G., Robustelli, P. & Shaw, D. E. Water Dispersion Interactions Strongly Influence Simulated Structural Properties of Disordered Protein States. *J. Phys. Chem. B* **119**, 5113–5123 (2015).
53. Abraham, M. J. *et al.* GROMACS: High performance molecular simulations through multi-level parallelism from laptops to supercomputers. *SoftwareX* **1–2**, 19–25 (2015).
54. Hornak, V. *et al.* Comparison of multiple Amber force fields and development of improved protein backbone parameters. *Proteins Struct. Funct. Bioinforma.* **65**, 712– 725 (2006).
55. Best, R. B., de Sancho, D. & Mittal, J. Residue-Specific α-Helix Propensities from Molecular Simulation. *J.* **102**, 1462–1467 (2012).

56. Best, R. B. & Hummer, Optimized Molecular Dynamics Force Fields Applied to the Helix−Coil Transition of Polypeptides. *J. Phys. Chem. B* **113**, 9004–9015 (2009).
57. Lindorff-Larsen, K. *et al.* Improved side-chain torsion potentials for the Amber ff99SB protein force field. *Proteins Struct. Funct. Bioinforma.* NA-NA (2010) doi:10.1002/prot.22711.
58. Berendsen, H. J. C., Postma, J. P. M., van Gunsteren, W. F., DiNola, & Haak, J. R. Molecular dynamics with coupling to an external bath. *J. Chem. Phys.* **81**, 3684–3690 (1984).
59. Evans, D. J. & Holian, B. L. The Nose–Hoover thermostat. *Chem. Phys.* **83**, 4069– 4074 (1985).
60. Nosé, S. A unified formulation of the constant temperature molecular dynamics methods. *Chem. Phys.* **81**, 511–519 (1984).
61. Parrinello, M. & Rahman, Polymorphic transitions in single crystals: A new molecular dynamics method. *J. Appl. Phys.* **52**, 7182–7190 (1981).
62. Rappsilber, J., Ishihama, & Mann, M. Stop and Go Extraction Tips for Matrix- Assisted Laser Desorption/Ionization, Nanoelectrospray, and LC/MS Sample Pretreatment in Proteomics. *Anal. Chem.* **75**, 663–670 (2003).
63. Klann, K., Tascher, G. & Münch, C. Functional Translatome Proteomics Reveal Converging and Dose-Dependent Regulation by mTORC1 and eIF2α. *Cell* **77**, 913-925.e4 (2020).
64. Willforss, J., Chawade, A. & Levander, F. NormalyzerDE: Online Tool for Improved Normalization of Omics Expression Data and High-Sensitivity Differential Expression Analysis. *Proteome Res.* **18**, 732–740 (2019).
65. Tyanova, S. *et al.* The Perseus computational platform for comprehensive analysis of (prote)omics data. *Methods* **13**, 731–740 (2016).
66. Mosmann, T. Rapid colorimetric assay for cellular growth and survival: Application to proliferation and cytotoxicity assays. *Immunol. Methods* **65**, 55–63 (1983).
67. Onafuye, H. *et al.* Doxorubicin-loaded human serum albumin nanoparticles overcome transporter-mediated drug resistance in drug-adapted cancer cells. *Beilstein Nanotechnol.* **10**, 1707–1715 (2019).
68. Corman, V. M. *et al.* Detection of 2019 novel coronavirus (2019-nCoV) by real-time RT-PCR. *Eurosurveillance* **25**, (2020).
69. Zhang, X., Ding, L. & Sandford, A. J. Selection of reference genes for gene expression studies in human neutrophils by real-time PCR. *BMC Mol. Biol.* **6**, (2005).
70. Moll, H. P., Maier, T., Zommer, A., Lavoie, T. & Brostjan, C. The differential activity of interferon-α subtypes is consistent among distinct target genes and cell *Cytokine* **53**, 52–59 (2011).

Figures

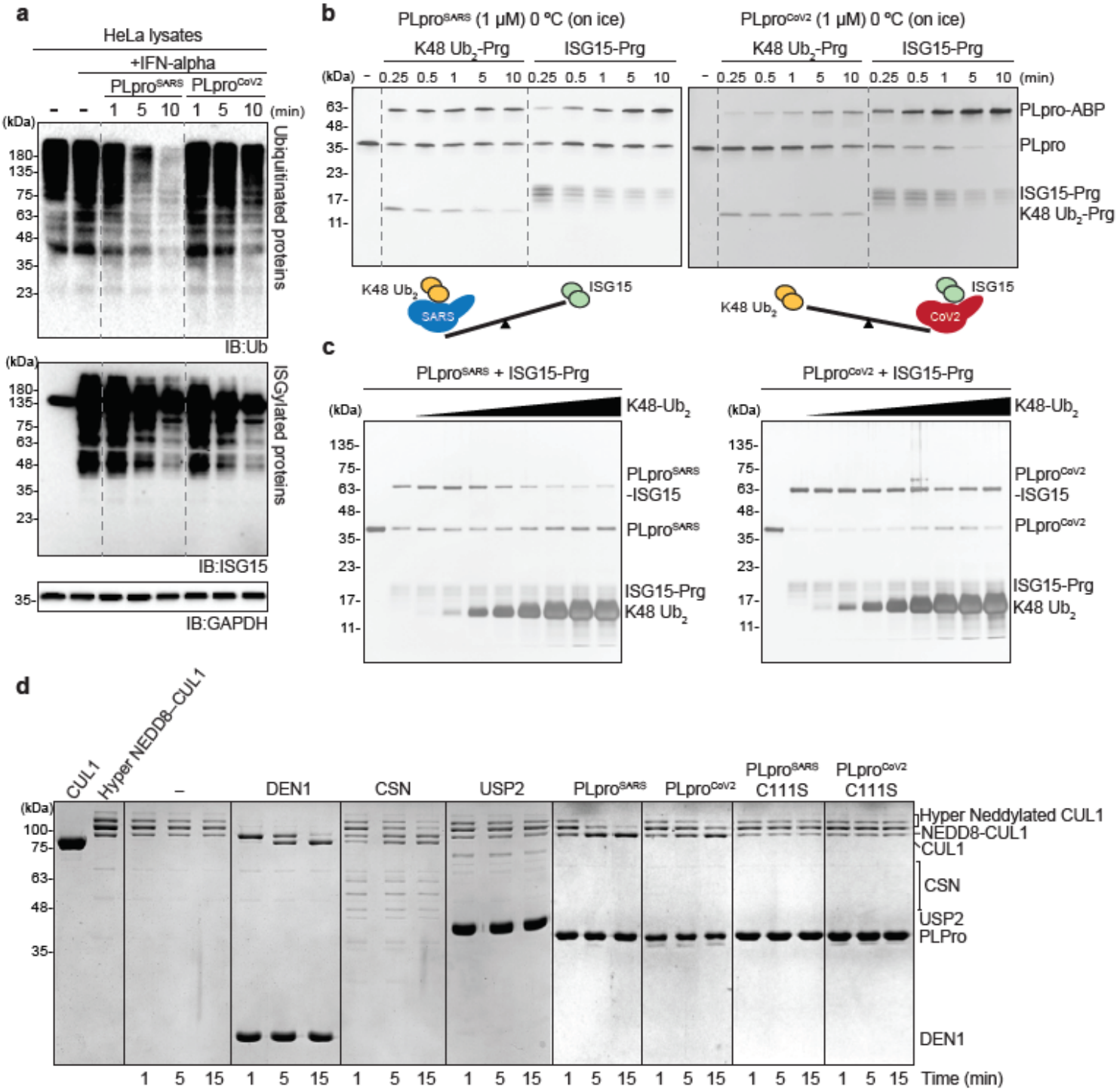

Figure 1

Comparison deISGylating and deubiquitylating activities of PLproSARS and PLproCoV2. a, HeLa cells were treated with IFN-β to induce ISGylation. Lysates were incubated with purified PLpro for indicated time points at 37°C. b, Purified PLpro from SARS (left) or SARS-CoV2 (right) were incubated with K48-Ub2 or ISG15 propargyl activity-based probes for indicated time points. c, Purified PLpro from SARS (left) or SARS-CoV2 (right) were pre-incubated with increasing amount of non-hydrolysable K48-Ub2 and

incubated with ISG15-prg on ice. d, Hyper-NEDDylated CUL1-RBX1 was incubated with purified DEN1, CSN, USP2 or PLpro proteins for indicated time points at 37°C.

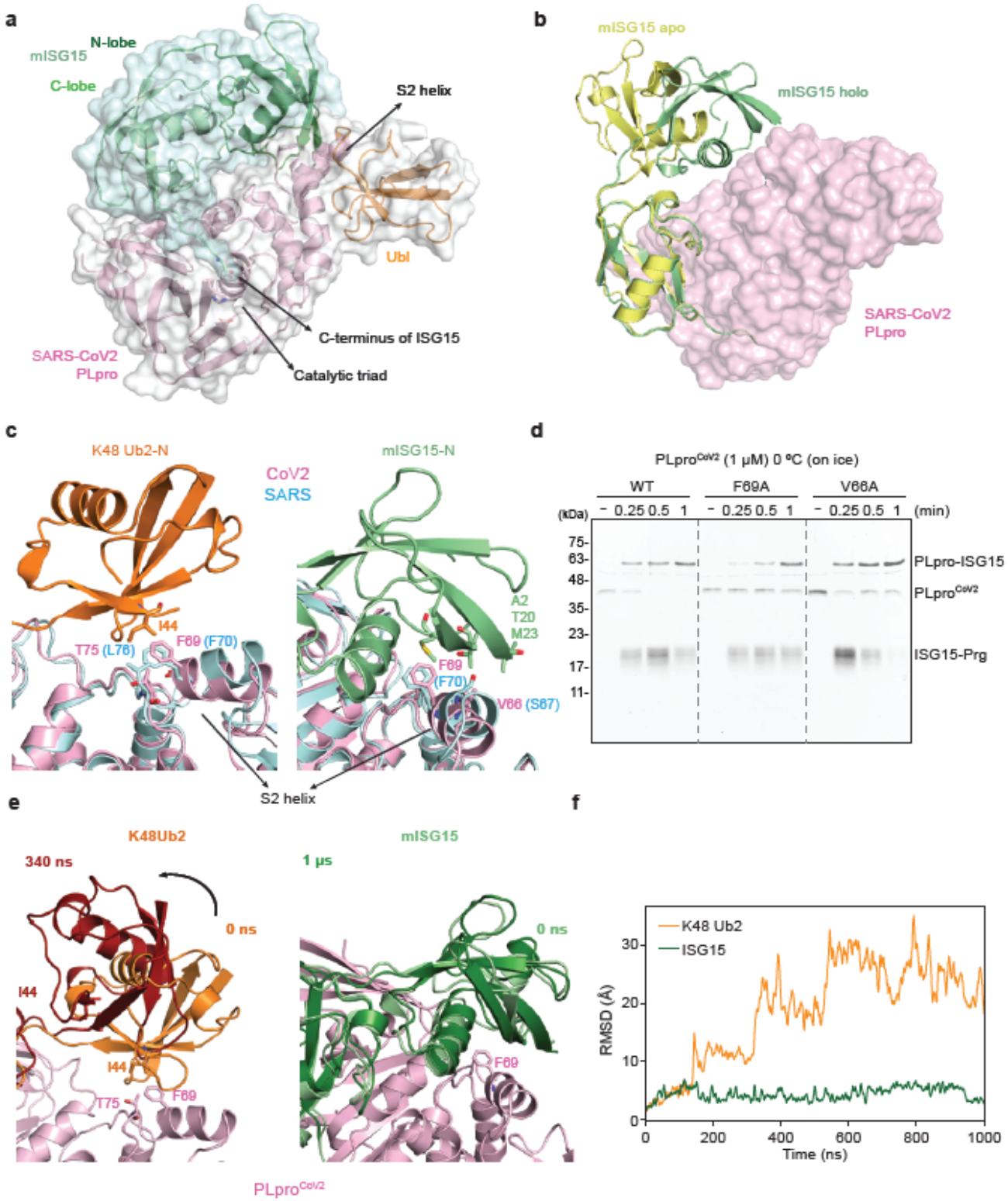

Figure 2

Structural analysis of SARS-CoV-2 PLpro in complex with 251 full length ISG15 a, Crystal structure of SARS-CoV-2 PLproC111S in complex with full-length murine ISG15 (mISG15) were presented as surface and cartoon model. C-terminal glycine of mISG15 and catalytic triad of PLproCoV2 were highlighted as

stick model. Ubiquitin like domain (Ubl) of PLpro were coloured in orange. b, Comparison of apo-mISG15 with mISG15 in complex with PLproCoV2. C-terminal domain of apo-mISG15 (PDB ID: 5TLA) was superimposed with mISG15 from PLproCoV2 complex structure. PLproCoV2 was presented as surface model. c, Comparison of K48-Ub2:PLproSARS complex structure (PDB ID: 5E6J) with mISG15:PLproCoV2. Residues forming hydrophobic interactions between N-terminal domain of K48-Ub2 or mISG15 and PLpro from SARS or SARS-CoV-2 were highlighted as stick model. d, Purified PLproCoV2 and mutants were incubated with ISG-propargyl probes for indicated time points. e, Snapshots from molecular dynamics simulations of PLproCoV2 (light pink cartoon) with (left) K48-Ub2 at 340 ns and (right) mISG15 at 750 ns. Key residues in the interface are highlighted. f, Backbone RMSD of the distal ubiquitin in K48-Ub2 (orange) and of the N-terminal domain of mISG15 (green) from their respective PLproCoV2-bound starting structures as function of time. The RMSD was calculated after superimposing the helix backbone atoms of PLproCoV2.

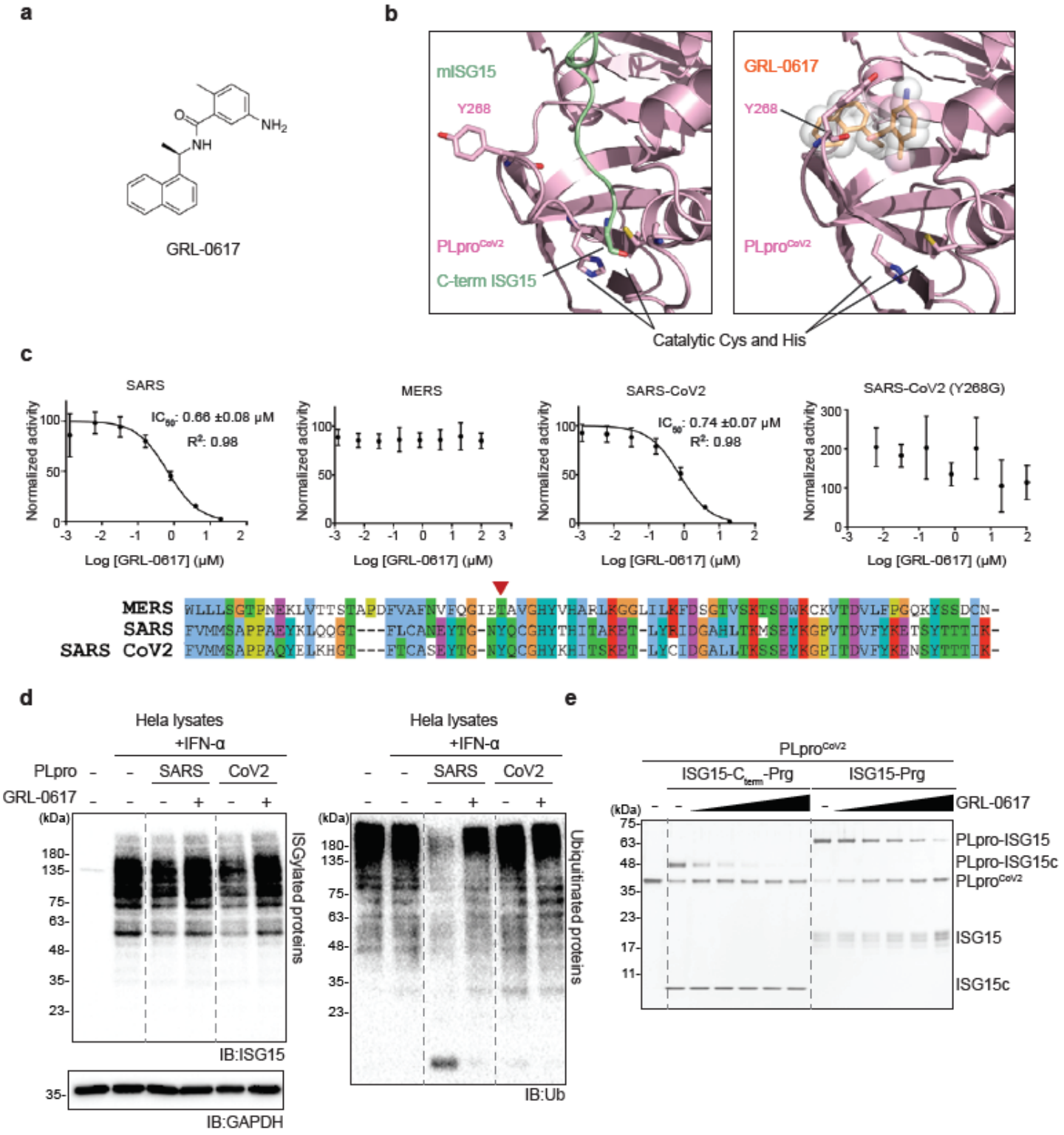

Figure 3

Effect of GRL-269 0617 inhibitor on PLproCoV2 a, Chemical structure of GRL-0617. b, Comparison of (left) ISG15-bound and (right) GRL-0617 bound structure. PLproCoV2:GRL-0617 complex structure was modelled based on GRL- 0617 bound PLProSARS structure (PDB ID: 3E9S). GRL-0617-interacting residue (Tyr268) and catalytic Cys, His of PLpro were highlighted as stick model. c. In vitro PLpro inhibition assay. Initial velocity of AMC release from ubiquitin-AMC in different concentration of GRL-0617 was

measured and normalized against to DMSO control. IC50 of GRL-0617 to PLproSARS and PLproCoV2 were presented. Data are presented as mean ± S.D (n=3). d, Effects of GRL-0617 on (left) deISGylase or (right) deubiquitinase activity of PLpro of SARS and SARS-CoV-2. e, Effects of GRL-0617 on PLproCoV2 activity to (left) ISG15c or (right) ISG15 propargyl activity based probes. Inhibitory effect of GRL-0617 on ISG15 was tested with various concentration of GRL-0617 (0-400 μM).

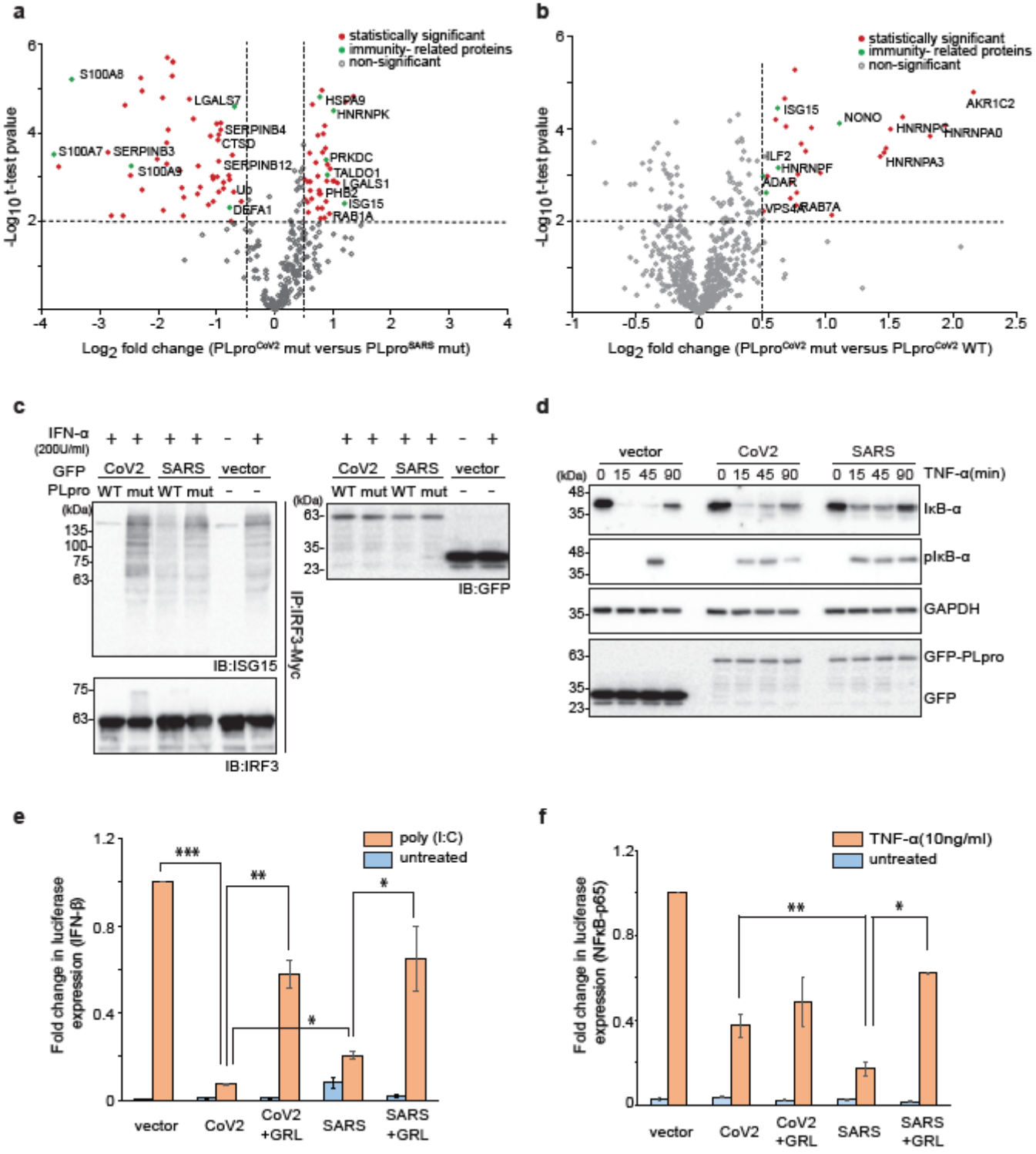

Figure 4

Effect on PLPs on 282 IRF3 and IkB pathways a, b Interactome of (a) PLproCoV2/PLproSARS and (b) PLproCoV2 mut/ PLproCoV2 wild-type. Statistically significant- and immunity-related- proteins were highlighted. c, IRF3 deISGylation activity of PLpro. A549 cells were co-transfected with Myc-IRF3 and wild-type or catalytically-inactive mutant of GFP-PLproCoV2 or GFP-PLproSARS. IRF3 were immuno precipitated and analysed with indicated antibodies. d, Effect of PLpro on NF-kB pathway. A549 cells were transfected with GFP-PLproCoV2 or GFP-PLproSARS and treated with TNF-α to induce IκB-α phosphorylation and degradation. e, f, Effect of PLpro on (e) IFN-β or (f) NF-κB expression level. A549 cells were transfected with indicated GFP-PLpro and treated with either poly (I:C) or TNF-α to induce IFN-β and NF-κB expression, respectively. Fold changes of luciferase level were presented. Data are presented as mean ± S.D (n=3). * $p < 0.1$, ** $p < 0.01$, *** $p < 0.001$.

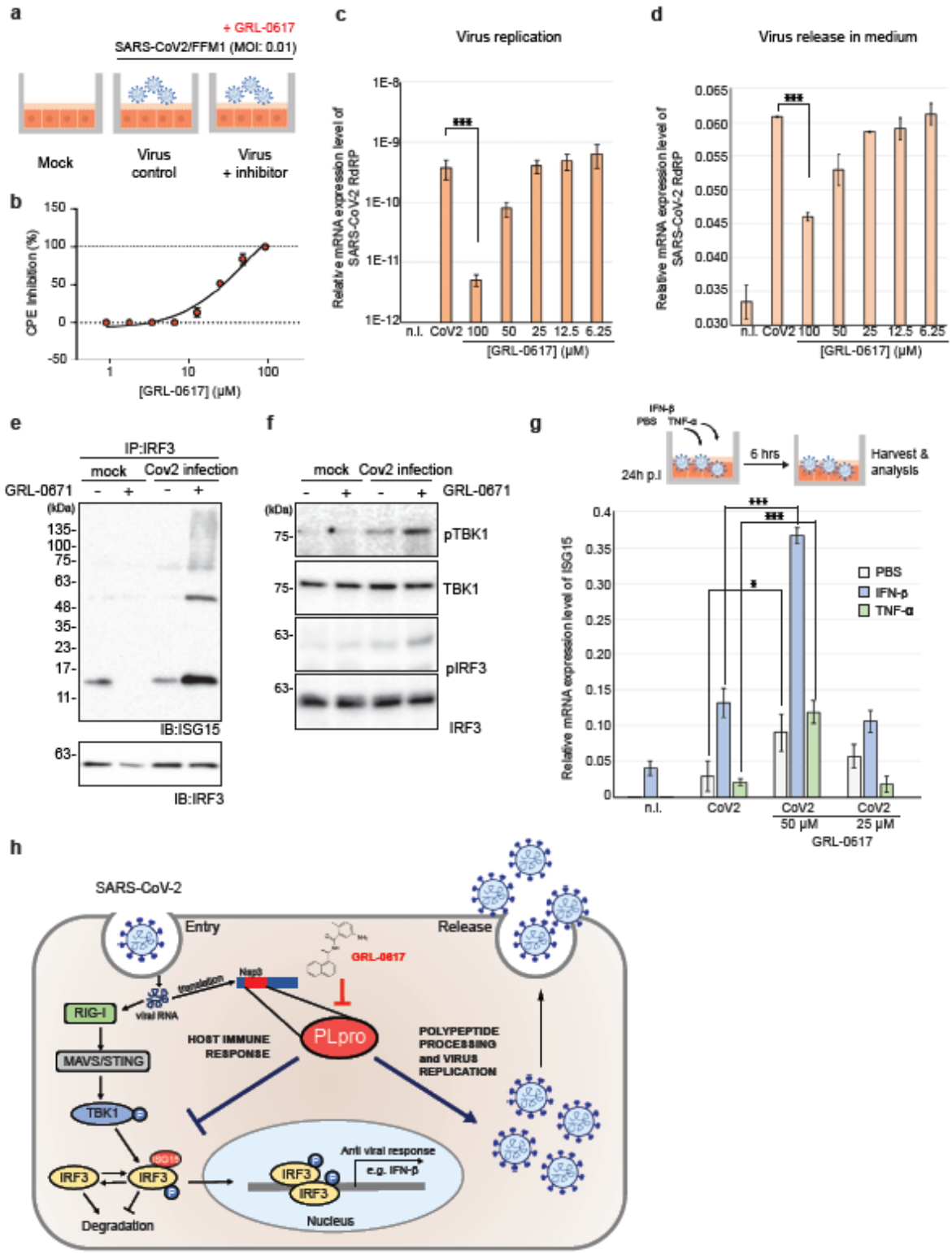

Figure 5

Inhibitory effects of 295 GRL-0617 on SARS-CoV2 a, Illustration of SARS-CoV-2 growth inhibition test with GRL-0617. b, CPE inhibition rate of GRL-0617 on SARS-CoV2 infected CaCo-2 cells. c, Intracellular virus production was analyzed by measuring SARS-CoV-2 RdRP mRNA level. Relative expression level of RdRP mRNA level was normalized to cellular GAPDH level. d, SARS-CoV-2 virus release in culture medium was analyzed by measuring RdRP mRNA level. e,f, The effect of GRL-0617 on IFN301 pathway. CaCo-2 cells

were infected with SARS-CoV-2 with or without GRL-0617. (e) Endogenous IRF3 were immunoprecipitated and analysed by immunoblotting. (f) Phosphorylation of TBK1 level were analysed by immunoblotting. g, Intracellular RNA was isolated from infected and uninfected cells treated with GRL-0617, IFN-β, TNFα as indicated. Relative ISG15-levels were analysed in a qRT-PCR analysis and normalized to ACTB levels. h, The roles of SARS-CoV-2 PLpro in their life cycle. Physiological roles of PLproCoV2 in both host-immune response and polypeptide processing are shown. Inhibition of PLpro by GRL-0617 is also presented. Data are presented as mean ± S.D (n=3). * $p < 0.1$, *** $p < 0.001$.

Supplementary Files

This is a list of supplementary files associated with this preprint. Click to download.

- rs27134v1supplementary.pdf